Contactless mechanical stimulation of tissue engineered constructs: Development and validation of an air-pulse device

Hugo Marchal-Chaud, Romain Rieger, van Than Mai, Edwin-Joffrey Courtial, Mélanie Ottenio, Catherine Bonnefont-Rebeix, Karine Bruyère, Caroline Boulocher

Contactless mechanical stimulation of tissue engineered constructs: development and validation of an air-pulse device.

Hugo Marchal-Chaud [a], Romain Rieger [a,b], Van Than Mai [a,b], Edwin-Joffrey Courtial [c], Mélanie Ottenio [d], Catherine Bonnefont-Rebeix [a], Karine Bruyère [d], Caroline Boulocher [e].

[a] *Univ. Lyon, VetAgro Sup, UPSP ICE 2021. A104, 1 Av. Bourgelat, 69280 Marcy l'Etoile, France.*

[b] *Univ. Lyon, École Centrale de Lyon, 36 Av. Guy de Collongue, 69134 Ecully, France,*

[c] *3d. FAB, Univ Lyon, Université Lyon1, CNRS, INSA, CPE-Lyon, ICBMS, Villeurbanne Cedex, France,*

d Univ Lyon, Univ Gustave Eiffel, Univ Claude Bernard Lyon 1, LBMC UMR_T9406, F-69622 Lyon, France

[e] *Institut Polytechnique UniLaSalle, Collège vétérinaire, Campus de Rouen, France*

1 Introduction

Tissue engineering (TE) is the study and development of biological substitutes to restore, maintain or improve tissue function [1,2]. TE is a multidisciplinary field that merges engineering and life science for the development of biocompatible and biomimetic tissue substitutes by using cells, growth factors and scaffolds. The ultimate goal of TE is to avoid the need to replace damaged tissue by stimulating or enhancing tissue repair and regeneration [3]. TE is motivated by three main health care issues, namely, the reliability of animal testing, the organ shortage crisis and drug development, which suffers from numerous failures during preclinical study phases (9 over 10) [4–6].

Despite over 30 years of research, tissue engineered constructs (TECs) still present differences in mechanical and biological properties compared to native tissue [7–10]. The microstructure and mechanical properties of biological tissues are mainly determined by the extracellular matrix (ECM). Mechanotransduction is the process through which mechanical stimulation triggers proliferation, apoptosis, and ECM synthesis, among other cell activities [11]. Regarding that aspect, the effect of *in vitro* stimulations such as compression, stretching, bending or fluid shear stress loading modalities have been extensively studied [12]. Dynamic compressive or stretching strain has been shown to induce gene expression related to the collagen metabolism involved in ECM synthesis, especially in TECs based on fibroblastic cells [13–15], stromal cells [16] or mesenchymal stem cells [17–20]. Regardless of the cell origin, to induce extracellular matrix synthesis, the mechanical stimulation frequency is usually set to 1 Hz [13,15–17,21], which corresponds to the human walking frequency. In these studies, the strain level ranged from 5 to 60% [13,15–17] depending on the scaffold and the cell type. It is therefore paramount to be able to regulate the stimulation frequency and the strain level with respect to the TEC studied.

To date, the devices used for these stimulations are largely represented by systems in direct contact with the TEC, and there are few studies on "noncontact" stimuli [22,23]. A fluid flow used to produce noncontact mechanical stimulation induced by an air pulse could be easily achieved *in vivo* without altering the tissue integrity. In addition, *in vivo,* epithelial cells have apical access to ambient air, such as the intestinal or female reproductive tract epithelium. Air-liquid interface cell cultures have been shown to be effective for the growth and differentiation of cultured epithelia, such as corneal, nasal, middle ear, intestinal or gastric cells [24–26]. Air exposure combined with mechanical stretch stimulation, mimicking the *in vivo* keratinization mechanism, has been studied in a 3D culture system and provided encouraging results towards artificial skin substitutes [27]. However, although air exposure and mechanical stress are the typical methods for cornification of skin equivalents or keratinization, the effect of air as a mechanical stimulus medium for cell culture and, with greater reason, for TEC maturation remains to be determined.

The objective of the study was to develop and validate a new air-pulse device for contactless and controlled mechanical simulation of a TEC. Our hypothesis was that the development of a contactless stimulation device with controlled mechanical parameters could be used during the maturation of scaffold-free TECs despite their initial fragility. The device was designed to deliver an air pulse that is controlled, calibrated, and maintains the sterility of the system within a noncytotoxic custom-made bioreactor. This study was conducted in the following three phases: 1) conception of the controlled air-pulse device combined with a 3D printed bioreactor; 2) experimental and numerical mechanical characterization of the air-pulse impact by digital image correlation (DIC); and 3) achieving sterility and noncytotoxicity of the air-pulse and of the 3D printed bioreactor using a novel dedicated sterilization process.

2 Materials and methods

2.1 Conception of the controlled air-pulse device combined with a 3D printed bioreactor

2.1.1 Air-pulse control and monitoring

The schematic diagram of the air-pulse stimulation device is described in Figure 1. The air was extracted from the laboratory compressed air system and filtered through a Beko Clearpoint® (BEKO TECHNOLOGIES, Sarreguemines, France) air filter. The air was then regulated upstream with a pressure controller before being delivered through a servo-controlled solenoid valve. The air pulse was then separated into two streams to stimulate two TECs simultaneously.

The resulting volumetric flow rate and the pressure were measured for each stream using an air flow metre SMC PFM7 (SMC Corporation, Tokyo, JAPAN) and a pressure sensor WIKA A-10 (WIKA, Klingenberg am Main, Germany). The air-pulse was conducted through a flexible polyamide and polyurethane tube with a 4 mm internal diameter and 1 m length and filtered once with a 0.2 µm filter before entering the incubator. The air flow was filtered a second time 1 m downstream before being finally pulsed into the bioreactor and onto the TEC. An acquisition card driven by a homemade program written with LabVIEW v2019 software was used to control and monitor the air pulse.

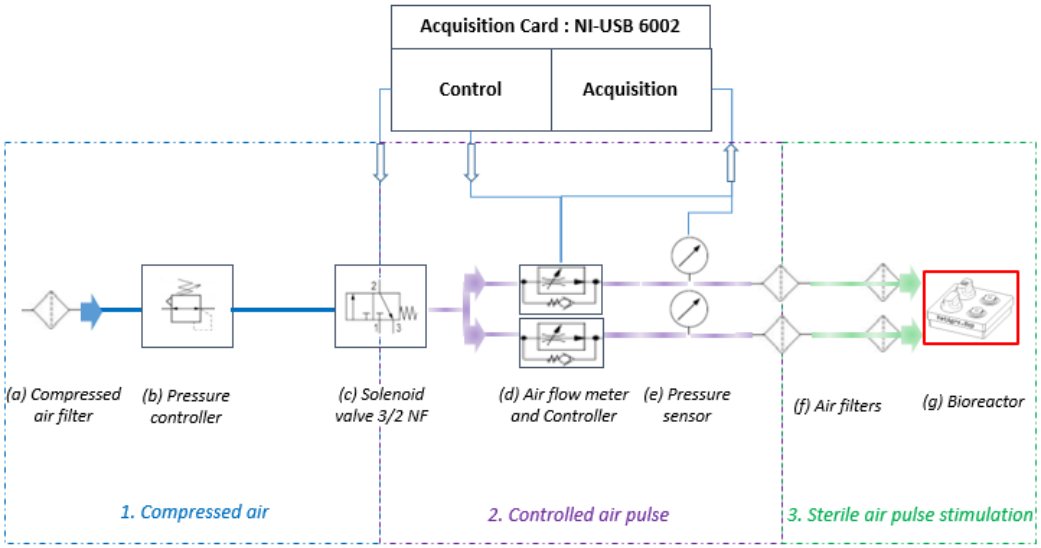

Figure 1: Schematic diagram of the air-pulse device. Air pressure is regulated (1). Then, the opening time of the solenoid valve is controlled to deliver an air pulse (2) before being filtered and sterilized in the bioreactor (3).

2.1.2 Air-pulse velocity at the nozzle outlet

The pipe lengths, the filters used to sterilize the air, and the delayed opening time of the solenoid valve influence the pressure and airflow losses from the input command to the nozzle outlet. An airflow metre and pressure sensor were used at the nozzle outlet to measure the maximum pressure and airflow losses during the pulse as a function of (i) the length, (ii) the pressure set, and (iii) the opening time of the solenoid valve to characterize the velocity of the air pulse at the nozzle outlet entering the bioreactor.

2.1.3 3D printed bioreactor conception

A dedicated bioreactor (70x70x40 mm) was designed using SolidWorks v2019. The prototyping was constructed with the use of a 3D printer (Ender 3 Max from CREALITY, Madrid, Spain) using fused deposition modelling (FDM) technology with a 1.75 mm polylactic acid (PLA) filament from SUNLU (Guangdong, P.R. China). This biopolymer was chosen because it is noncytotoxic and widely used for medical applications [28–30]. The 3D printed bioreactor consisted of the following six different parts (Figure 2): the upper part, which includes inserts to plug the nozzle tip to hold the needle or the sterile cap to ensure sterility; the lower part, which maintains the TEC; the overall sterility was maintained by an autoclaved 20 mm diameter O-ring (BGS technic KG, Wermelskirchen, Germany) placed between the upper part and the nozzle tip or the sterile cap.

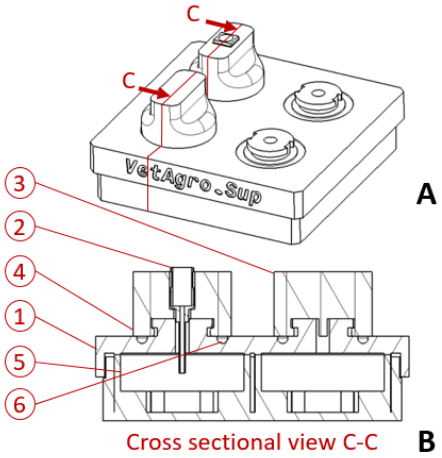

Figure 2: Schematic of the 3D printed bioreactor. A. General overview. B. Cross-sectional view C-C: (1) upper part, (2) nozzle, (3) sterile cap, (4) nozzle tip, (5) lower part, (6) O-ring.

2.2 Mechanical characterization of the air-pulse impact

2.2.1 Manufacture of the speckled silicone substitutes

LSR 4305 silicone (Elkem, Oslo, Norway) was used as a physico-chemical inert substitute for the TEC since it is isotropic, homogeneous, and incompressible and since it does not dry out under an air pulse. This specific silicone was chosen due to its Young's modulus, which is a similar that of *in vivo* tissues such as skin (222 kPa [31]) or cartilage (varying from 0.02 to 6.44 MPa [32]). Components A and B (which contained the catalyst) were mixed 1:1 with 0.5% white matt paint from a do-it-yourself store. The preparation was poured into a 30 cc syringe and centrifuged before being weighed and poured into a 100 mm diameter petri dish to reach a height of 2 mm. After polymerization for 24 hours at 60 °C at a pressure of 700 mBar, light speckling by droplet deposition was performed on the surface using black aerosol paint for further displacement field measurement by DIC. Samples of 15 mm diameter by 2 mm height were cut with a punch for mechanical characterization of the substitute.

2.2.2 Mechanical characterization of the silicone substitute

Dynamic mechanical analysis (DMA) was performed on 4 samples of the silicone substitute using an oscillatory compression test at 25 °C (DHR2, TA instrument, USA) [33]) with a 15 mm parallel plate geometry. This method was chosen because it can also be performed on a TEC with a low elastic modulus (from a Pa to a few kPa).

The measurements of two oscillatory signals (force and displacement) provided the compression storage E' and loss E'' moduli. First, the linear region was determined at a constant frequency (data not shown), then a frequency test from 0.1 Hz to 10 Hz was performed at a constant strain (1%), which provided the linear viscoelastic region. The resulting storage and loss moduli curves were fitted by a second-order generalized Maxwell model to extract the Young's modulus E_0 and the overall viscosity η_0. This procedure is described more extensively in a previous work [34].

2.2.3 Surface displacement during air-pulse using digital image correlation (DIC)

The displacement field on the surface of the silicone substitute was measured during the application of the air-pulse by a DIC study, as described in Figure 3A. The air-pulse stimulation device was used to deliver air pulses controlled by the LabVIEW interface via a nozzle held by a system designed and 3D printed specifically for the study.

Two synchronized high-speed cameras (SA3, Photron®, with an image size of 512 x 512 pixels), mounted with a pair of 105 mm lenses, were set up to record the area of interest (approximately 15 x 15 mm²) at a frame rate of 2000 images/s. Exposure time, aperture, and light intensity were chosen to obtain a good contrast and enough depth of field to ensure a good focus on the surface during the air-pulse application. Calibration of the setup and digital image correlation were performed using VIC3D software (VIC3D, version 8, Correlated Solution). The pixel size was approximately 0.05 mm. Computation was performed with a subset size of 23 pixels and a step of 5 pixels.

The 3D reconstruction of the silicone surface was obtained in a coordinate system for which the (x, y) plane was tangent to the initial silicone plane. The results mainly focused on the altitude (Z) and the displacement normal to the surface (W) of all points and the major Lagrange strain field.

To synchronize the recording of the images and the air-pulse, a transistor-transistor logic (TTL) signal was sent to trigger the recording of the cameras and to the air-pulse system acquisition card.

An image of the silicone surface before the air-pulse was applied was selected as the initial frame. During the application of the air-pulse, the silicone surface was deformed in a well-shape, as described in Figure 3B. The point J was defined as the well bottom. During the stabilized phase of a given air pulse, its location in the (x, y) plane was stable. An average stimulation frame was selected in this stabilized phase to analyse the well shape. Twenty depth profiles were extracted from planes $\mathcal{P}_i(J, \vec{u}_i, \vec{z})$, where $\vec{u}_i = cos\,\theta_i\vec{x} + sin\,\theta_i\vec{y}$, $\theta_i = \frac{\pi\, i}{20}$ and $i \in [1,20]$. After θ_i clockwise rotation, these profiles were plotted in the same plane (x, z).

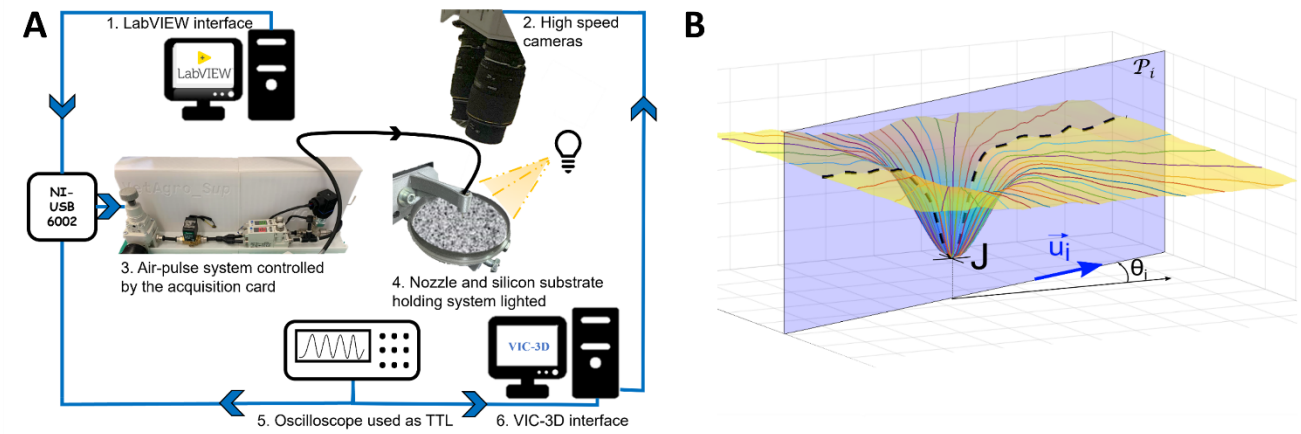

Figure 3: DIC study. A. Schematic diagram of the DIC experiment. B. Graphical representation of the methodology followed to extract 20 depth profiles.

2.2.4 Numerical simulation of the air-pulse mechanical stimulation

To assess the mechanical effect of the air pulse on a TEC, a numerical simulation was developed in Comsol Multiphysics (version 5.3, COMSOL, Inc.). A fully coupled fluid-structure interaction (FSI) approach was used to model the impact of the air-pulse on the TEC represented by the silicone substitute. Due to the axial symmetry of the problem and to enhance computation time, axisymmetric modelling was used. A stationary analysis was performed to compare the numerical surface displacement profile of the substitute induced by a stabilized volumetric air flow rate to the DIC data acquired at a stabilized surface displacement profile.

The model described in Figure 4 is composed of (i) a fluid domain D1, which represents the air with a box of 20 mm radius (in axisymmetric representation) and 36 mm height, with material properties from the Comsol toolbox and (ii) a solid domain D2, which represents the silicone substitute with a box of 15 mm radius (in axisymmetric representation) and 2 mm height with material properties determined from DMA. The nozzle is represented by its boundary conditions BC1 (inlet mass flow rate, $Q_{sv} = 2.1e^{-4}\ m^3/s$ experimentally characterized) and BC3 (inner wall with no-slip boundary condition) with a 2 mm inlet radius for a 8 mm height and a 0.5 mm outlet radius for a 14 mm height. The computed domain is closed by a fluid boundary condition BC2 (atmospheric pressure) and a wall BC4 with no slip condition, a flat support condition BC5 ($\boldsymbol{U} \cdot \boldsymbol{e_z} = 0$) and an embedding BC6 ($\boldsymbol{U} = \boldsymbol{0}$) at the point $r = z = 0$ to prevent rigid body motion, with $\boldsymbol{U}$ being the solid displacement. The fluid-structure interaction is described by a fully coupled interface BC7. A finer physics-controlled mesh generated on the geometry by Comsol was used and provided a total of 26°293 triangle elements.

For the fluid domain (D1), the Reynolds and Mach numbers were computed to design the numerical study, which were $Re = \frac{Q_{sv} \times d \times \rho}{S * \mu} = 2.56\text{e}^4$ and $Ma = \frac{Q_{sv}}{S \times a} = 1{,}12$, respectively, where $d = 1\,mm$ is the diameter of the nozzle outlet, $S = 0.8\,mm^2$ is the surface of the nozzle outlet, $\mu = 1.849e^{-5}\ \text{kg}/m.s$ is the dynamic viscosity of the fluid, $\rho = 1.184\ \text{kg}/m^3$ is the density of the fluid and $a = 343\,m/s$ is the speed of sound in air. The Reynolds Averaged Navier–Stokes (RANS)-based turbulence models were used to describe the fluid domain of a stationary compressible mean flow (Eq. 1), where ρ_f is the fluid density, p is the mean pressure, $\boldsymbol{v}$ is the fluid velocity vector, μ is the dynamic viscosity, μ_T is the turbulent viscosity, $\boldsymbol{K}$ is the viscous stress tensor, $\boldsymbol{F}$ is the external forces applied to the fluid and $\boldsymbol{I}$ is the identity tensor. The accuracies of the two-equation turbulence models (k-ε and k-ω) were compared for the prediction in the impinging jet modelling [35,36]. The standard two-equation k-ε model was then chosen, as illustrated in the results and discussion sections.

$$\rho_f(\boldsymbol{v} \cdot \nabla \boldsymbol{v}) = \nabla \cdot [-p\boldsymbol{I} + \boldsymbol{K}] + \boldsymbol{F}; \quad \nabla \cdot (\rho_f \boldsymbol{v}) = 0; \qquad \textit{Eq. 1}$$

$$\boldsymbol{K} = (\mu + \mu_T)\left(\nabla \boldsymbol{v} + (\nabla \boldsymbol{v})^T - \frac{2}{3}(\nabla \cdot \boldsymbol{v})\boldsymbol{I}\right)$$

For the solid domain (D2), experimental tensile tests on the silicone performed for a strain <100% (data not shown) in two perpendicular directions demonstrated a linear behaviour. Moreover, the viscous behaviour was considered negligible because of its very low overall viscosity η_0, as described in the results section. Therefore, the silicone substitute was modelled as an isotropic linear elastic material using Hooke's law with elastic modulus E=210 kPa measured experimentally using DMA (cf. results section), Poisson's ratio = 0.49 (to enable numerical convergence instead of 0.5 classically used for elastomers) and density $\rho_s = 1.09\,\mathrm{g.cm} - 3$ (from the manufacturer data sheet). Elastostatic equations were used to solve the solid part (Eq. 2), with $\boldsymbol{\sigma}$ as the Cauchy stress tensor, $\boldsymbol{f}_V$ as the volume force vector, $\mathbb{C}$ as the stiffness tensor, $\boldsymbol{\varepsilon}$ as the small strain tensor and $\boldsymbol{u}$ as the solid displacement vector.

$$\boldsymbol{\sigma} + \boldsymbol{f}_V = \mathbf{0}; \quad \boldsymbol{\sigma} = \mathbb{C}{:}\boldsymbol{\varepsilon}; \quad \boldsymbol{\varepsilon} = \frac{1}{2}(\nabla \boldsymbol{u} + (\nabla \boldsymbol{u})^T) \qquad \textit{Eq. 2}$$

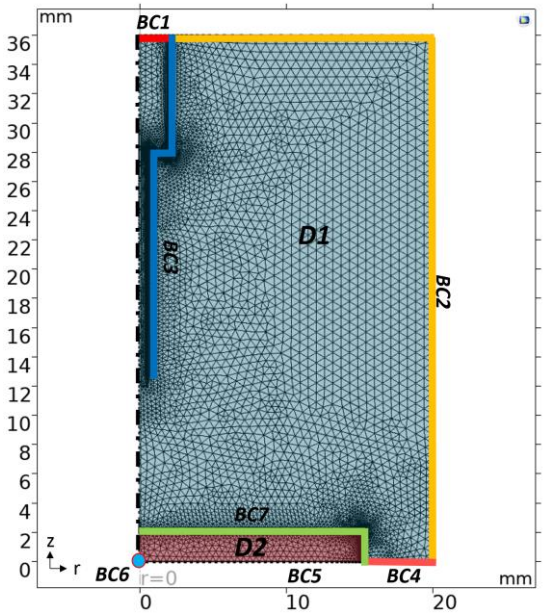

Figure 4: Mesh and boundary conditions of the axisymmetric numerical model. The fluid domain (D1), which represents the air, is in green blue. The solid domain (D2), which represents the TEC (silicone substitute), is in red. BC1 is the inlet condition ($Q = 2.1e^{-4}\ m^3/s$), BC2 is the outlet boundary condition ($P = P_{atm}$), BC3 is the inner wall boundary condition (no-slip boundary condition), BC4 is a wall with slip condition, BC5 is the flat support condition, BC6 is the solid embedding point and BC7 is the fluid structure interaction interface (fully coupled).

2.2.5 Validation of the numerical model

The numerical results were compared to the vertical surface displacement profiles of the silicone measured on 20 cutting planes from 0 to 180° by DIC (Figure 6). First, over the radial interval r = [-4;4] mm, the experimental and numerical displacements, i.e., W^{exp} and W^{num}, respectively, were shifted so that $\min(|W^{exp}|) = min(|W^{num}|) = 0$. Since the radial coordinates r^{exp} differed between each experimental cutting plane, linear interpolation using a first-order Taylor formula was performed to compute the interpolated experimental displacement W^{int} for each cutting plane to plot them within the same radial interval $r^{num} = [-4; 4; 0.1]$, as described in Eq. 3.

$$\forall\, j \in [-4; 4; 0.1]\ \&\ k \in [r^{exp}] \mid (k-1) < j\ \&\ (k+1) > j\,,$$
$$W_j^{int} = W_{k-1}^{exp} + \left(r_j^{num} - r_{k-1}^{exp}\right) \times \frac{W_{k+1}^{exp} - W_{k-1}^{exp}}{r_{k+1}^{exp} - r_{k-1}^{exp}} \qquad \textit{Eq. 3}$$

Second, the mean interpolated experimental displacement profile $\overline{W^{int}} = \frac{\sum_{i=1}^{20} W_i^{int}}{20}$ was computed as the average of the 20 cutting planes.

Third, the comparison between the mean experimental displacement profile and the simulated one was performed using the coefficient of determination calculation described in Eq. 4 and by the difference between the area under the two curves using the rectangle method.

$$\forall \mathrm{j} \in [-4; 4; 0.1\}, \quad \mathrm{R}^2 = \frac{\sum_{\mathrm{j}=1}\left(W_j^{\mathrm{num}} - \overline{W^{int}}\right)^2 - \sum_{\mathrm{j}=1}\left(W_j^{\mathrm{num}} - W_j^{\mathrm{int}}\right)^2}{\sum_{\mathrm{j}=1}\left(W_j^{\mathrm{num}} - \overline{W^{int}}\right)^2} \qquad \textit{Eq. 4}$$

2.3. Sterility and noncytotoxicity of the device

2.3.1. Air-pulse sterility

The sterility of the air-pulsed through the nozzle was characterized. The air-pulse device was used to perform an air-pulse stimulation test under sterile conditions in a complete cell culture medium composed of 10% FBS (foetal bovine serum), 1% penicillin/streptomycin, 0.1% amphotericin B and DMEM Glutamax (Thermo Fisher Scientific, Waltham, Massachusetts, USA). The device was placed inside the incubator at 37 °C and 5% CO2 and the air-pulse stimulations occurred for 10 minutes once a day for 3 days and the device was left further for one week without stimulations. The cell culture medium was then collected and subjected to bacteriological analysis in the bacteriological Analysis Veterinary Laboratory (LAV, Marcy l'Etoile, France) through Gram staining, aerobic culture (Columbia blood agar with sheep blood medium, BioMérieux, Marcy l'Etoile, France), TSB (Tryptic Soy Broth, Bio-Rad, Hercules, California, USA) and thioglycolate broth (THIO-CLAIR, BioMérieux, Marcy l'Etoile, France) to assess the absence of contamination.

2.3.2. 3D printed bioreactor noncytotoxicity and sterility

The noncytotoxicity of the bioreactor was ensured using PLA, a biopolymer obtained from the fermentation of corn starch under the effect of bacteria producing lactic acid and used as a 3D printing material in FDM technology.

A dedicated homemade sterilization protocol for the printed bioreactor was developed. Since PLA has a glass transition temperature tg = 60 °C, the 3D printed bioreactor was immersed in a 70° ethanol bath for 72 hours and then autoclaved at 105 °C for 25 minutes. As the cytotoxicity of the printed Sunlu PLA+ material after thermochemical treatment has never been assessed, biological evaluations were needed. The study of the cytotoxicity of the autoclaved bioreactor was performed based on the ISO 10993-5 standard for *in vitro* cytotoxicity, as follows.

Mouse fibroblast cells from an L929 cell line were cultured in contact with the material for 72 hours. The L929 cell line was purchased from Sigma (Saint Louis, Missouri, USA) and used for the cytotoxicity assay of the printed material. Cells were thawed and seeded at 2500 cells/cm² in a T75 flask in a complete cell culture medium composed of 10% FBS (foetal bovine serum), 1% penicillin/streptomycin, 0.1% amphotericin B and DMEM Glutamax (Thermo Fisher Scientific, Waltham, Massachusetts, USA). The cells were incubated at 37 °C in a 95% humidified atmosphere (5% CO2). After 7 days of culture, the cells were harvested following a classic protocol with 5% EDTA trypsin and resuspended in a complete cell culture medium. A proliferation assay was previously performed for 3 days in a 6-well plate with varying concentrations of cells to obtain the optimum confluence of the cell monolayer. The cells were seeded at 2500 cells/cm² for the 3 groups-test, as follows: (1st group named: Control) a blank control where cells were seeded in a regular culture dish, (2nd group named: PLA) a direct contact where cells were seeded in a 3D printed PLA culture dish, and (3rd group named: Latex) a direct contact cytotoxic positive control where cells were seeded in a regular culture dish with a latex sample. All test conditions were performed three times in triplicate in 9.6 cm² wells (6-well plate) for 72 hours before the cells were trypsinized and enumerated with trypan blue. A BD Pharmingen apoptosis and mortality detection kit ANNEXIN V 7AAD was then used according to the manufacturer's instructions [37–39]. The cells were resuspended at a concentration of 10^6 cells/ml in a binding buffer solution. One hundred microlitres of this solution was drawn, and 5 µL each of ANNEXIN V and 7AAD staining solution was added. The cells were then analysed using a BD Accuri C6 Plus flow cytometry system to determine the cellular viability and, thus, determine the cytotoxicity of PLA. Cell apoptosis and mortality were analysed by Annexin V staining, and apoptosis was analysed by 7AAD staining. The morphology and granularity of the cells were analysed by flow cytometry. The data were collected upon 15,000 events per sample.

Statistical analysis was performed in R (R Foundation for Statistical Computing, Vienna, Austria), normality was checked using the Shapiro–Wilk normality test, and equal variance was checked using the Bartlett test. After assessment of normality of distributions and equal variance, a one-way ANOVA was performed with Tukey HSD as post hoc tests.

3. Results

3.1. Air-pulse monitoring

Figure 5 shows that the volumetric flow rate of the air-pulse measured at the output of the nozzle quickly stabilized after 100 ms for a set pressure of 2 bar and an opening time of the solenoid of 1 s. The value of $4.1e^{-4}$ m^3/s corresponding to the mean value of the plateau of the volumetric air flow rate curve was used as the inlet condition at the nozzle input for the numerical simulation.

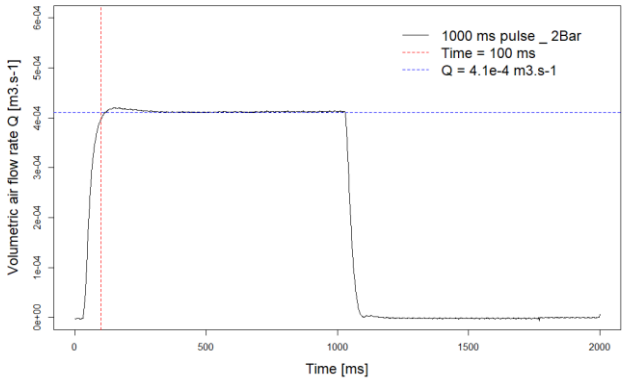

Figure 5: Volumetric air flow rate measured at the output of the nozzle for a set pressure of 2 bar and an opening time of the solenoid of 1 s.

3.2. Mechanical characterization of the air-pulse impact

3.2.1. Mechanical characterization of the silicone substitute

The elastic contribution (storage modulus) and viscous contribution (loss modulus) of the silicone were characterized by DMA (Figure 6A) as a function of the loading frequency, as illustrated in Figure 6B. Figure 6C displays the computed Young's modulus $E_0 = 210\ \mathrm{kPa}$ and overall viscosity $\eta_0 = 1.7\,e^{-4}\ \mathrm{kPa.s}$ obtained for the 4 samples characterized. The ratio between the mean viscosity and Young's modulus ${}^{E_0}/_{\eta_0} = 1.23\,e^{6}\ s^{-1}$ leads to ignoring the viscous contribution of the material. Therefore, the behaviour of the silicone substitute was modelled as a purely linear, isotropic and homogeneous elastic material with $E = 210\ \mathrm{kPa}, \nu = 0.49$ and $\rho_s = 1.07\ \mathrm{g}.cm^{-3}$ [40].

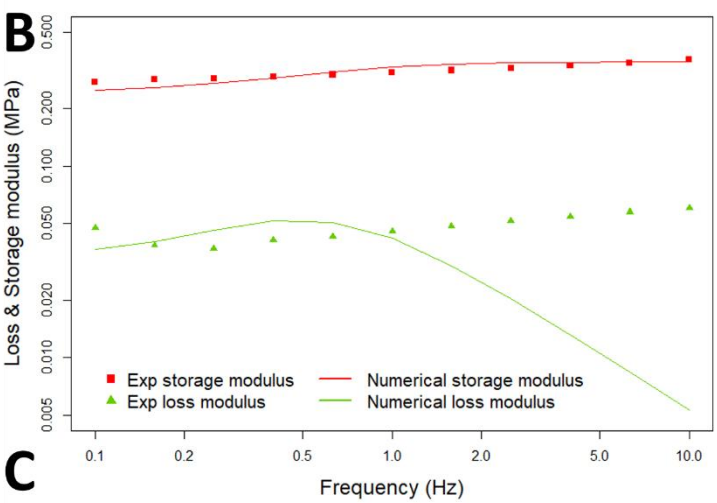

C

Silicone sample	E_0 [kPa]	η_0 [kPa.s]
Mean	**210**	**1.7E-4**
SD	*6.9*	*15.9E-6*

Figure 6: Results of the dynamic mechanical analysis: A. DMA system with a sample represented in pink; B. experimental data (dotted lines) and fitted numerical results (solid lines) of the storage modulus (red) and the loss modulus (green); C. mean values of the mechanical parameters computed for the 4 silicone samples.

3.2.2. Surface displacement during air-pulse impact using DIC

The different air pulses applied on the silicone surface are clearly visible in the normal displacement W for the well-bottom J, always reaching the same depth under pressure, and its location in the plane (x, y) remains stable. However, it did not recover its initial position between the different air pulses (17.2 ± 0.4 µm difference between 5 pulses). The 3D reconstruction of the silicone surface corresponding to the initial frame and the average stimulation frame are given in Figure 7. Figure 7A shows that the silicon surface before the air pulse is applied is not perfectly plane in the impact zone (magnitude of 134 ± 8µm between the extrema). At the average stimulation frame, the point J defined at the well bottom moved 190.1 ± 2.9 µm from the initial frame. However, the effect of the air-pulse was not axisymmetric on the Z profile; thus, an ellipse was indeed predicted at the air-pulse impact, as depicted in Figure 7B.

Major Lagrange strain distributions are mapped on the 3D silicone surface in Figure 7C. The major and minor strain values did not exceed 1.28% and 0.06%, respectively, and the maxima did not coincide with the well bottom J. A vector field of the major strains is also provided in Figure 7D, as indicated by white arrows superimposed on a Z map of the silicone surface. The vector field described an ellipse, and its focus seemed to be approximately at the well bottom position.

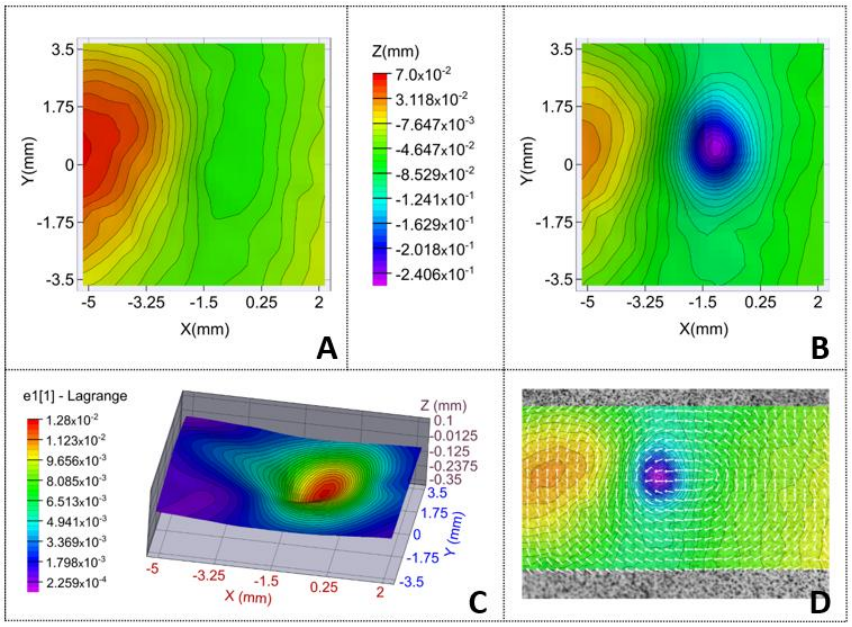

Figure 7: Surface deformation of the silicon substitute under an air pulse. A & B. Surface altitude (Z) distribution: A. before air-pulse stimulation (initial frame) and B. under air-pulse stimulation (average stimulation frame). C. Major Lagrange strain distribution under air-pulse stimulation. D. Vector field of major Lagrange strains (white arrows) superimposed on the altitude (Z) distribution.

3.2.3. Numerical simulation of the air-pulse mechanical stimulation

The calculation converged in 86 seconds on a laptop (I7 processor with 2,6 GHz and 16 Go of RAM), and the segregated solver displayed error values for velocity, pressure, space referential coordinates, turbulence and displacement fields in the range of $10e^{-4}$ and $10e^{-5}$, as recommended to conclude on the convergence of the model [41]. The convergence of the model was also verified by the mass conservation study, and the calculated error between the ratio of the total mass flow and the output of the model was $e_{num} = 2\%$, which is below the relative tolerance $e_{tol} = 5\%$ (data not shown). The mesh convergence was studied by checking the maximal numerical displacement normalized by the maximal experimental displacement measured by DIC as a function of the number of elements. The model quickly converged to 1 for the k-ε turbulence model, as shown in Figure 8. The k-ω turbulence model diverged and reached a plateau with a maximum surface displacement four times greater than the experimental displacement. A simulation with a finer physics-controlled mesh made of 26°293 triangle elements with the k-ε turbulence model was therefore used for the comparison of the surface displacement profiles between the simulation and the DIC results, as illustrated in the next section.

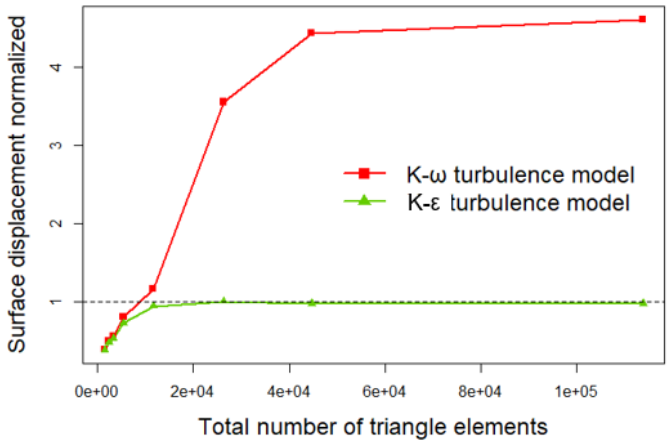

Figure 8: Mesh convergence study performed by checking the maximum surface displacement of the simulation normalized by the maximum experimental displacement value for the k-ω (red square) and k-ε (green triangle) turbulence models.

The simulated velocity profile along the axis of symmetry from the nozzle inlet to the surface of the silicone is illustrated in Figure 9Figure 1A, and the iso-value air flow velocity map is depicted in Figure 9B. The simulation gives a maximal velocity of $\boldsymbol{v} \cdot \boldsymbol{e_z} = 460\ \mathrm{m}.s^{-1}$ inside the nozzle, which decreases drastically to a velocity of $11.2\ \mathrm{m}.s^{-1}$ at the point of impact with the surface of the silicone substitute. The maximum displacement of the silicone surface due to the air flow was $W = 0.177\ \mathrm{mm}$ (raw data without shifting). A negative pressure gradient is observed along the surface of the silicone substitute during stationary flow.

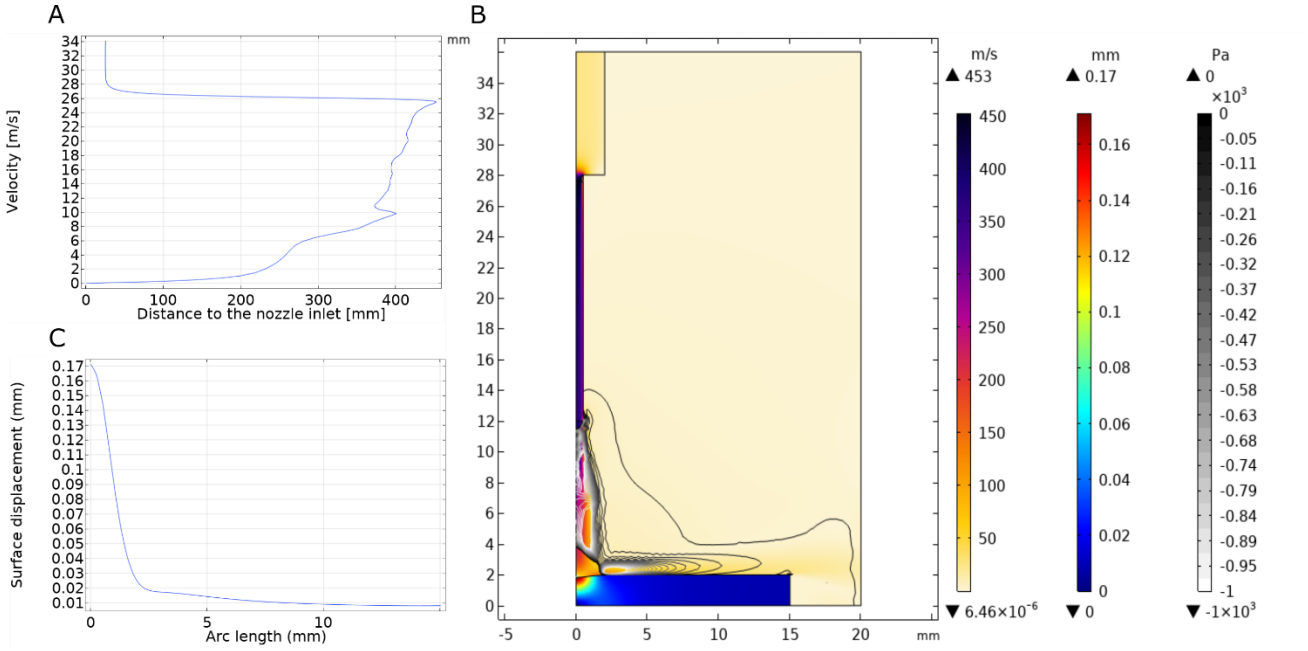

Figure 9: Numerical results of the fluid structure interaction study in stationary mode: A. air velocity profile (m/s) along the axis of symmetry, from the nozzle inlet to the silicone substitute surface; B. computed axisymmetric simulation of the fluid structure interaction; the contour of the fluid pressure is displaced from 0 to -100 Pa; C. surface displacement profile (mm) of the silicone substitute from the impact point to the edge.

3.2.4. Comparison of the experimental and numerical surface displacement profiles

The surface displacement profiles of the 20 cutting planes measured experimentally by DIC over a 4 mm radius around the centre of impact are depicted with the numerical profile in Figure 10. The numerical profile (red line) is very similar to the averaged experimental profile (black dashed line). The difference between the absolute maximum displacements of the averaged experimental data (0.156 mm) and the numerical result (0.155 mm) is 0.6%.

The coefficient of determination between the averaged experimental data and the numerical result of the surface displacement (black dashed line and red line, respectively) was $R^2 = 0.98$. The comparison of the area under the curve between these two profiles showed a difference of 4% over the interval r = [-2;2].

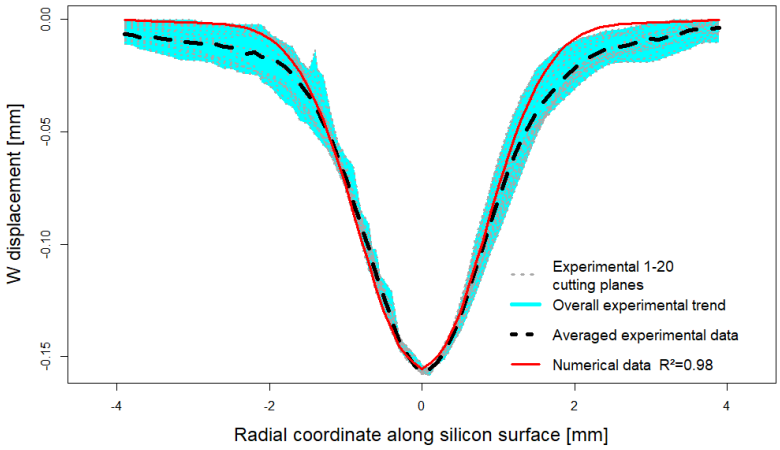

Figure 10: Comparison of the vertical displacement profiles along the surface of the silicone under an air pulse for the experimental data (20 cutting lines represented by grey dotted lines with the overall trend in cyan and the averaged curve, represented by the black dashed line) and the numerical result (red line). The experimental curves are not symmetric, which explains why they seemed to be below the numerical curve, and the minimum of the averaged experimental curve is different from zero.

3.3. Sterility and noncytotoxicity of the device

3.3.1. Air-pulse sterility

After one week, gross visual inspection of the phenol red in the medium as well as the microscopic observations showed no apparent contamination or change in pH of the medium for both the control and air-pulse samples. Further investigation with Gram staining and aerobic, aerobic TSB and anaerobic thioglycolate broth culture tests confirmed the absence of contamination, as summarized in Table 1.

	Gram staining	**Aerobic culture**	**Aerobic TSB**	**Anaerobic thioglycolate broth**
Air-pulse stimulation	Negative	Negative	Negative	Negative
Control	Negative	Negative	Negative	Negative

Table 1: Sterility analysis of the L929 cell line seeded at 2500 cells/cm² by Gram staining, aerobic culture, TSB (tryptic soy broth) and thioglycolate broth. The cells were stimulated for 3 days, 10 minutes once a day and incubated at 37 °C and 5% CO2 for a total incubation time of 7 days.

3.3.2. Noncytotoxicity of the autoclaved 3D printed bioreactor

After 72 hours of culture, flow cytometry analysis of living and nonapoptotic cells showed a significant difference (p-value < 0.0001) between Latex (cytotoxic positive control group) and PLA as well as Control (negative control group), as shown in Figure 11. There was no significant difference between PLA and Control.

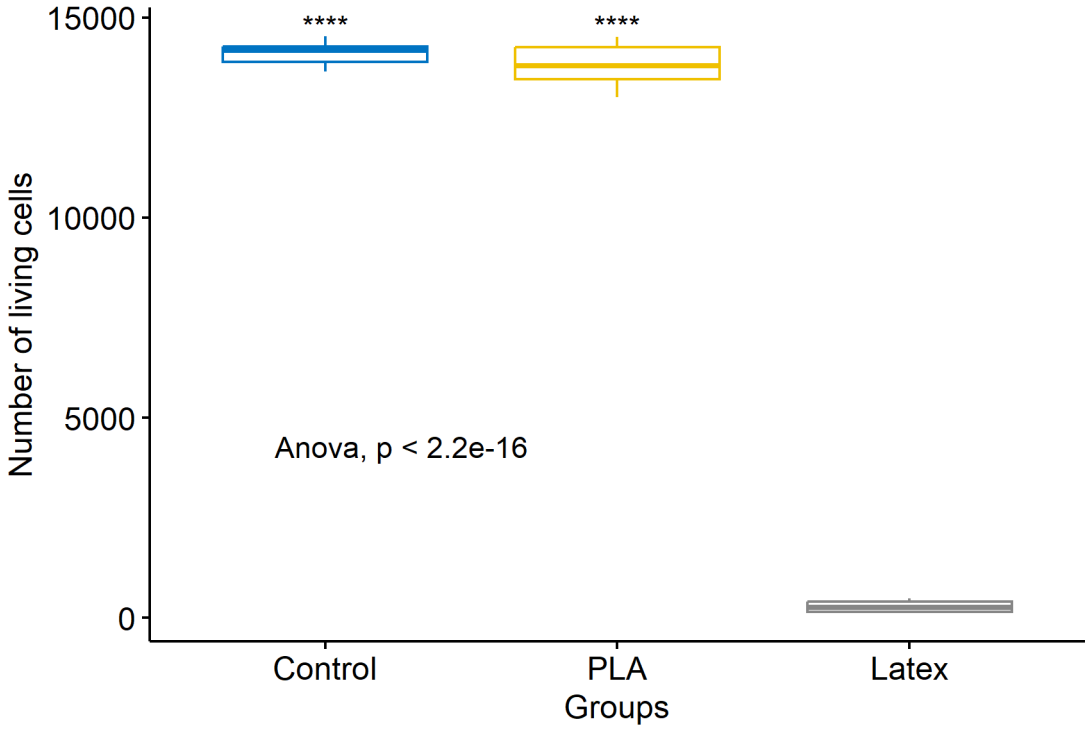

*Figure 11: Box plot of flow cytometry results of the cytotoxicity tests of the PLA. PLA group in direct contact was compared with the positive control (Latex) and the negative control (Control) for living and nonapoptotic L929 cells initially seeded at 2500 cells/cm². ****: p- value < 0.0001. The cells were incubated for 72 hours at 37 °C and 5% CO2.*

4. Discussion

The study was primarily focused on the development of an air-pulse device prior to its use on TEC for a long-term goal of using air-pulse stimulation for *in vivo* applications (*e.g.,* epithelia). Our hypothesis was that the development of a noncytotoxic contactless stimulation device with controlled mechanical parameters could make it possible to achieve effective and noninvasive mechanical stimulation of TECs. To be able to do so, a controlled air-pulse device was first developed. Then, we characterized the mechanical stimulation of the air-pulse impact both experimentally and numerically. Finally, the sterility of the air pulse and the noncytotoxicity of the homemade 3D-printed bioreactor were assessed. The developed numerical model will make it possible to further estimate the micromechanical phenomenon induced by air-pulse stimulation of a TEC, which are impossible to directly measure, leading to changes in cellular activity during maturation. Additionally, the simulation could be used to estimate and adjust the air-pulse parameters with respect to the evolution of the TEC's mechanical properties during maturation to achieve the desired surface displacement profile of the TEC.

Sterility and noncytotoxicity of the device must be strictly assured to avoid any contamination and perturbation in cellular responses for further use with TECs. Regarding the sterility of the air-pulse (Table 1), the results showed that there was no contamination in a 3-day time period of experimentation, which illustrates a well-designed stimulation work-flow, as illustrated in Figure 1. However, since the developed device was not directly placed in an incubator, contamination due to repetitive manipulation of the bioreactor is inevitable if strict sterile conditions are not respected by the operator.

PLA is widely used for prototyping by 3D printing and has been demonstrated to be biocompatible and noncytotoxic [28–30] in addition to being biodegradable [28]. A novel sterilization process for PLA was developed in this study based on a thermochemical process. We demonstrated that the treated PLA was noncytotoxic and did not influence cell proliferation (Figure 11). Furthermore, the initial shape of the 3D-printed bioreactor was preserved (data not shown). The absence of cytotoxicity due to the sterilization process might be due to an additional esterification reaction during the autoclave of the PLA at 105 °C for 25 minutes [42]. This reaction is probably caused by the immersion in the 70° ethanol bath for 72 hours, which finalizes the cross-linking of the polymer and preserves the initial shape. To confirm the effect of the chemical reaction of the ethanol bath on the PLA, a specific study should be performed to fully characterize the chemical phenomenon that preserves the geometry of the 3D printed object after autoclaved sterilization. Additionally, since the maturation period can be longer than 14 days for TEC maturation [19,43,44], further noncytotoxicity tests over a

longer period should be performed. In addition, further investigations such as proteomic profiling including chemokines and cytokines profiling, should also be conducted to verify that cellular metabolism is not impaired, in order to assess the biocompatibility of PLA according to the dedicated application [45,46].

A silicone material (LSR 4305) was used to characterize the mechanical behaviour of the air-pulse impact because of the stability over time of its mechanical properties [47,48]. DMA tests were performed to characterize the viscoelastic properties of the silicone, concluding that the viscous part can be neglected regarding the elastic part for frequencies within the range of 0.1 to 10 Hz, which corresponds to the mechanical stimulation frequency of the air-pulse, as discussed below.

The surface displacement of the silicone substitute induced by the air pulse was characterized by DIC. Since the viscous part was negligible, to prevent oscillatory effects of the silicone surface induced by a short air pulse, which could complicate the DIC analysis, a stabilized air flow at the nozzle outlet was achieved by opening the solenoid valve for a long time period [49]. A solenoid valve opening timespan of 1000 ms was chosen, which is 10 times higher than the air flow rate stabilization time (Figure 5). The major Lagrangian strain values of the silicone surface computed from DIC did not exceed 1.28% (Figure 7C). These results indicate that the silicone substitute under the air-pulse behaves as a perfectly linear elastic material and was modelled as such in the numerical simulation.

Experimentally, between each air pulse, a mean vertical residual displacement with respect to the initial configuration state was observed. This partial displacement recovery could be explained by the adhesion of the silicone on its support in the deformed configuration state, preventing a complete return to its initial (undeformed) configuration state. This partial displacement recovery (which represents 9% of the maximum displacement) should be prevented in immersion conditions corresponding to the real situation for TEC maturation, where DIC might not be possible due to important rigid body motion and cell culture medium refractive index and colour altering the image correlation.

The mean value of the raw maximum displacement of the 20 silicone surface displacement profiles analysed every 9° from 0 to 180° during a pulse was $0.190 \pm 9.7e^{-5} mm$ (data not shown). The areas under the curves were calculated for each of the 20 experimental profiles, and the difference between each profile varied from 0.05% to 8.2%. The lack of axial symmetry, also illustrated by the elliptical shape of the impact observed on the surface displacement 2D map (Figure 7B), cannot be explained by the anisotropic behaviour of silicone, as conventional silicone materials are isotropic, but it can be explained by the nonnormality of the nozzle with the silicone surface during the pulse and the nonplanarity of the initial surface.

For high Reynolds numbers, Reynolds-averaged Navier–Stokes (RANS)-based turbulence models can be used to model a fluid exiting a nozzle on a wall, called an impinging jet, to describe the heat transfer phenomenon [35,36]. Impinging jets are schemed by different regions from the outlet to the wall, as follows: core region, developing region, fully developed region, stagnation region and wall jet region. Each region designates a specific fluid-flow profile where physical phenomena are better described in regard to the chosen turbulence model. To the best of our knowledge, very few studies have dealt with impinging jets on a deformable wall using FSI. Direct numerical simulations, large eddy simulations (LESs) or even hybrid RANS/LESs would be the most suitable numerical methods to describe the complex FSI involved in impinging jets on a deformable wall. However, those methods are very difficult to implement and are very costly in terms of the computation time needed. Additionally, in this study, we were only interested in the averaged displacement profile of the solid part and were not concerned with the effect of the solid part on the fluid velocity. Therefore, we have chosen the most commonly used two-equation turbulence models for engineering problems, which have been shown to well describe shear stress and pressure at the wall [35]. In this study, the two-equation turbulence models (k-ε and k-ω) were compared to assess the computed solid displacement profile against experimental data from DIC. The maximum surface displacement in the k-ε turbulence model converges rapidly to the experimental value (Figure 8). The k-ω turbulence model overestimates the experimental values. These results show that the k-ε turbulence model is better able to describe the solid displacement profile induced by an impinging jet with a low Reynolds number on a deformable body with an elastic modulus on the order of hundreds of kPa. Further investigations could be performed to study the relation between the air flow velocity and the solid displacement profile under immersed conditions in a cell culture medium corresponding to the real situation for TEC maturation. Additionally, a wider range of elastic and visco-elastic properties should be investigated to consider the variability of TEC mechanical behaviours.

The raw numerical surface displacement profile showed a maximum of 0.177 mm at the stagnation point (arc length = 0) and an overall minimum of 0.016 mm at the right edge of the solid part compared to the initial surface configuration in the steady state (Figure 9C). The nonnull displacement along the whole solid surface and especially at the right edge can be explained by a nonnull pressure induced by the stationary flow along the surface of the solid [50], as depicted by the pressure contour lines in Figure 9B. Therefore, to compare the numerical to the experimental displacement profiles, their minimums were adjusted such that $\min(|W_i^{\exp}|) = min(|W^{num}|) = 0$ (where $i \in [1,20]$ represents each experimental silicone surface displacement profile line *cf.* Figure 3B), and the entire curves were shifted accordingly. The comparison between the numerical and averaged experimental profiles (red line and black dashed line, respectively, as depicted in Figure 10) gives a coefficient of determination $R^2 = 0.98$ and a difference of 4% between the areas under the curves. From these results, it can be concluded that the numerical simulation provides a predictable

surface displacement profile. Therefore, the numerical simulation could be used to study the micromechanical effects induced by an air pulse and to adjust the air flow rate to the maximum surface displacement desired on a TEC.

5. Conclusion

This study led to the development and characterization of a calibrated air-pulse device for TEC mechanical stimulation during maturation. To fully decipher the mechanical stimulation induced by an air pulse, it was characterized by DIC, and a numerical twin of the device was developed. Since the mechanical properties of the TEC evolve during the maturation process, the numerical model allows us to adjust the air-pulse parameters according to the desired surface displacement of the TEC. In addition, the numerical model can be used to investigate the micromechanical effects of air pulses inside the TEC, which cannot all be measured experimentally, for instance, wave propagation generated during the air-pulse impact. Linking the biological response and the micromechanical effects generated during air-pulse stimulation will improve our understanding of the cellular response to mechanical stimulation. An ethanol/autoclaved sterilization protocol for 3D printed objects in PLA has been developed in this study, enabling the use of 3D printing in cell culture. Further studies remain to be conducted to ensure that PLA is noncytotoxic and that the incubator environment does not affect its properties over periods of more than one month related to the characteristics of TEC maturation. The device can be used to study the cell response to contactless cyclic mechanical stimulation, particularly in TECs with fibroblasts, stromal cells and mesenchymal stem cells, which have been shown to be sensitive to the frequency and strain level at the air-liquid interface.

References

[1] R. Langer, J. Vacanti, Tissue engineering, Science. 260 (1993) 920–926. https://doi.org/10.1126/science.8493529.

[2] R. Skalak, C.F. Fox, Tissue Engineering: Proceedings of a Workshop, Held at Granlibakken, Lake Tahoe, California, February 26-29, 1988, Liss, 1988. https://books.google.fr/books?id=jY2BAAAAIAAJ.

[3] R.M. Nerem, Tissue engineering: the hope, the hype, and the future, Tissue Eng. 12 (2006) 1143–1150. https://doi.org/10.1089/ten.2006.12.1143.

[4] P. Greaves, A. Williams, M. Eve, First dose of potential new medicines to humans: how animals help, Nat Rev Drug Discov. 3 (2004) 226–236. https://doi.org/10.1038/nrd1329.

[5] Organ Donation and Transplantation, Human Rights Channel. (2022). https://human-rights-channel.coe.int/organ-donation-en.html (accessed August 8, 2022).

[6] A.S. Khalil, R. Jaenisch, D.J. Mooney, Engineered tissues and strategies to overcome challenges in drug development, Adv Drug Deliv Rev. 158 (2020) 116–139. https://doi.org/10.1016/j.addr.2020.09.012.

[7] A. Vedadghavami, F. Minooei, M.H. Mohammadi, S. Khetani, A. Rezaei Kolahchi, S. Mashayekhan, A. Sanati-Nezhad, Manufacturing of hydrogel biomaterials with controlled mechanical properties for tissue engineering applications, Acta Biomaterialia. 62 (2017) 42–63. https://doi.org/10.1016/j.actbio.2017.07.028.

[8] F. Han, J. Wang, L. Ding, Y. Hu, W. Li, Z. Yuan, Q. Guo, C. Zhu, L. Yu, H. Wang, Z. Zhao, L. Jia, J. Li, Y. Yu, W. Zhang, G. Chu, S. Chen, B. Li, Tissue Engineering and Regenerative Medicine: Achievements, Future, and Sustainability in Asia, Frontiers in Bioengineering and Biotechnology. 8 (2020). https://www.frontiersin.org/articles/10.3389/fbioe.2020.00083 (accessed September 1, 2022).

[9] M.B. Wandel, C.A. Bell, J. Yu, M.C. Arno, N.Z. Dreger, Y.-H. Hsu, A. Pitto-Barry, J.C. Worch, A.P. Dove, M.L. Becker, Concomitant control of mechanical properties and degradation in resorbable elastomer-like materials using stereochemistry and stoichiometry for soft tissue engineering, Nat Commun. 12 (2021) 446. https://doi.org/10.1038/s41467-020-20610-5.

[10] A.K. Gaharwar, I. Singh, A. Khademhosseini, Engineered biomaterials for in situ tissue regeneration, Nat Rev Mater. 5 (2020) 686–705. https://doi.org/10.1038/s41578-020-0209-x.

[11] P.A. Sundaram, ed., Title page, in: Mechanotransduction, Academic Press, 2021: pp. i–iii. https://doi.org/10.1016/B978-0-12-817882-9.00012-4.

[12] T.D. Brown, Techniques for mechanical stimulation of cells in vitro: a review, Journal of Biomechanics. 33 (2000) 3–14. https://doi.org/10.1016/S0021-9290(99)00177-3.

[13] M. Zhao, L. Li, B. Li, D. Wu, C. Zhou, Y. Tian, A Comparative Study of Fibroblast Behaviors under Cyclic Stress Stimulus and Static Culture on 3D Patterned Matrix, Journal of Bionic Engineering. 10 (2013) 148–155. https://doi.org/10.1016/S1672-6529(13)60209-7.
[14] A.S. Peters, G. Brunner, T. Krieg, B. Eckes, Cyclic mechanical strain induces TGFβ1-signalling in dermal fibroblasts embedded in a 3D collagen lattice, Arch. Dermatol. Res. 307 (2015) 191–197. https://doi.org/10.1007/s00403-014-1514-2.
[15] J.C. Shelton, D.L. Bader, D.A. Lee, Mechanical conditioning influences the metabolic response of cell-seeded constructs, Cells Tissues Organs (Print). 175 (2003) 140–150. https://doi.org/10.1159/000074630.
[16] J.K. Mouw, J.T. Connelly, C.G. Wilson, K.E. Michael, M.E. Levenston, Dynamic compression regulates the expression and synthesis of chondrocyte-specific matrix molecules in bone marrow stromal cells, Stem Cells. 25 (2007) 655–663. https://doi.org/10.1634/stemcells.2006-0435.
[17] V. Terraciano, N. Hwang, L. Moroni, H.B. Park, Z. Zhang, J. Mizrahi, D. Seliktar, J. Elisseeff, Differential response of adult and embryonic mesenchymal progenitor cells to mechanical compression in hydrogels, Stem Cells. 25 (2007) 2730–2738. https://doi.org/10.1634/stemcells.2007-0228.
[18] K. Sakao, K.A. Takahashi, Y. Arai, A. Inoue, H. Tonomura, M. Saito, T. Yamamoto, N. Kanamura, J. Imanishi, O. Mazda, T. Kubo, Induction of chondrogenic phenotype in synovium-derived progenitor cells by intermittent hydrostatic pressure, Osteoarthr. Cartil. 16 (2008) 805–814. https://doi.org/10.1016/j.joca.2007.10.021.
[19] K.T. Shalumon, H.-T. Liao, C.-Y. Kuo, C.-B. Wong, C.-J. Li, M. P.a., J.-P. Chen, Rational design of gelatin/nanohydroxyapatite cryogel scaffolds for bone regeneration by introducing chemical and physical cues to enhance osteogenesis of bone marrow mesenchymal stem cells, Materials Science and Engineering: C. 104 (2019) 109855. https://doi.org/10.1016/j.msec.2019.109855.
[20] R.D. Sumanasinghe, S.H. Bernacki, E.G. Loboa, Osteogenic differentiation of human mesenchymal stem cells in collagen matrices: effect of uniaxial cyclic tensile strain on bone morphogenetic protein (BMP-2) mRNA expression, Tissue Eng. 12 (2006) 3459–3465. https://doi.org/10.1089/ten.2006.12.3459.
[21] J.T. Slocum, P. Ascoli, N. Bandiera, B. Katz, S. Kataria, M. Wentworth, N. Monteiro, E. Smith, K. Weekes, B. Johnstone, P.C. Yelick, Design and validation of a device for the mechanical stimulation of bioengineered 3D neo-tissue constructs, Precision Engineering. 64 (2020) 129–137. https://doi.org/10.1016/j.precisioneng.2020.03.020.
[22] B.A. Zelle, H. Gollwitzer, M. Zlowodzki, V. Bühren, Extracorporeal Shock Wave Therapy: Current Evidence, Journal of Orthopaedic Trauma. 24 (2010) S66. https://doi.org/10.1097/BOT.0b013e3181cad510.
[23] A. Ramirez, J. Schwane, C. Mcfarland, B. Starcher, The effect of ultrasound on collagen synthesis and fibroblast proliferation in vitro, Medicine and Science in Sports and Exercise. 29 (1997) 326–32. https://doi.org/10.1249/00005768-199505001-00294.
[24] S. Chen, J. Schoen, Air-liquid interface cell culture: From airway epithelium to the female reproductive tract, Reproduction in Domestic Animals. 54 (2019) 38–45. https://doi.org/10.1111/rda.13481.
[25] S. Klasvogt, W. Zuschratter, A. Schmidt, A. Kröber, S. Vorwerk, R. Wolter, B. Isermann, K. Wimmers, H.-J. Rothkötter, C. Nossol, Air–liquid interface enhances oxidative phosphorylation in intestinal epithelial cell line IPEC-J2, Cell Death Discov. 3 (2017) 1–7. https://doi.org/10.1038/cddiscovery.2017.1.
[26] C. Nossol, A.-K. Diesing, N. Walk, H. Faber-Zuschratter, R. Hartig, A. Post, J. Kluess, H.-J. Rothkötter, S. Kahlert, Air–liquid interface cultures enhance the oxygen supply and trigger the structural and functional differentiation of intestinal porcine epithelial cells (IPEC), Histochem Cell Biol. 136 (2011) 103–115. https://doi.org/10.1007/s00418-011-0826-y.
[27] M.H. Jung, S.-M. Jung, H.S. Shin, Co-stimulation of HaCaT keratinization with mechanical stress and air-exposure using a novel 3D culture device, Sci Rep. 6 (2016). https://doi.org/10.1038/srep33889.
[28] K. Hamad, M. Kaseem, H.W. Yang, F. Deri, Y.G. Ko, Properties and medical applications of polylactic acid: A review, Express Polym. Lett. 9 (2015) 435–455. https://doi.org/10.3144/expresspolymlett.2015.42.

[29] E.H. Tümer, H.Y. Erbil, Extrusion-Based 3D Printing Applications of PLA Composites: A Review, Coatings. 11 (2021) 390. https://doi.org/10.3390/coatings11040390.
[30] A.G. Morozov, D.A. Razborov, T.A. Egiazaryan, M.A. Baten'kin, D.Ya. Aleynik, M.N. Egorikhina, Y.P. Rubtsova, I.N. Charikova, S.A. Chesnokov, I.L. Fedushkin, In Vitro Study of Degradation Behavior, Cytotoxicity, and Cell Adhesion of the Atactic Polylactic Acid for Biomedical Purposes, J Polym Environ. 28 (2020) 2652–2660. https://doi.org/10.1007/s10924-020-01803-x.
[31] G. Constantinides, Z.I. Kalcioglu, M. McFarland, J.F. Smith, K.J. Van Vliet, Probing mechanical properties of fully hydrated gels and biological tissues, J Biomech. 41 (2008) 3285–3289. https://doi.org/10.1016/j.jbiomech.2008.08.015.
[32] J. Antons, M.G.M. Marascio, J. Nohava, R. Martin, L.A. Applegate, P.E. Bourban, D.P. Pioletti, Zone-dependent mechanical properties of human articular cartilage obtained by indentation measurements, J Mater Sci Mater Med. 29 (2018) 57. https://doi.org/10.1007/s10856-018-6066-0.
[33] A. Zühlke, M. Gasik, N.E. Vrana, C.B. Muller, J. Barthes, Y. Bilotsky, E. Courtial, C. Marquette, Biomechanical and functional comparison of moulded and 3D printed medical silicones, Journal of the Mechanical Behavior of Biomedical Materials. 122 (2021) 104649. https://doi.org/10.1016/j.jmbbm.2021.104649.
[34] E.-J. Courtial, L. Fanton, M. Orkisz, P.C. Douek, L. Huet, R. Fulchiron, Hyper-Viscoelastic Behavior of Healthy Abdominal Aorta, IRBM. 37 (2016) 158–164. https://doi.org/10.1016/j.irbm.2016.03.007.
[35] F. Mercier, F. Golay, S. Bonelli, F. Anselmet, R. Borghi, P. Philippe, 2D axisymmetrical numerical modelling of the erosion of a cohesive soil by a submerged turbulent impinging jet, European Journal of Mechanics - B/Fluids. 45 (2014) 36–50. https://doi.org/10.1016/j.euromechflu.2013.12.001.
[36] A.M. Achari, M.K. Das, Application of various RANS based models towards predicting turbulent slot jet impingement, International Journal of Thermal Sciences. 98 (2015) 332–351. https://doi.org/10.1016/j.ijthermalsci.2015.07.018.
[37] E.J. Comparetti, G.G. Romagnoli, C.M. Gorgulho, V. de A. Pedrosa, R. Kaneno, Anti-PSMA monoclonal antibody increases the toxicity of paclitaxel carried by carbon nanotubes, Materials Science and Engineering: C. 116 (2020) 111254. https://doi.org/10.1016/j.msec.2020.111254.
[38] D.T. Humphreys, M.R. Wilson, MODES OF L929 CELL DEATH INDUCED BY TNF-α AND OTHER CYTOTOXIC AGENTS, Cytokine. 11 (1999) 773–782. https://doi.org/10.1006/cyto.1998.0492.
[39] B. Kloesch, T. Becker, E. Dietersdorfer, H. Kiener, G. Steiner, Anti-inflammatory and apoptotic effects of the polyphenol curcumin on human fibroblast-like synoviocytes, International Immunopharmacology. 15 (2013) 400–405. https://doi.org/10.1016/j.intimp.2013.01.003.
[40] Brochure_Silbione-Series.pdf, (n.d.). https://elkem.co.jp/wp-content/uploads/2015/03/Brochure_Silbione-Series.pdf (accessed September 26, 2022).
[41] I.B. Celik, Procedure for Estimation and Reporting of Uncertainty Due to Discretization in CFD Applications, J. Fluids Eng. 130 (2008) 078001. https://doi.org/10.1115/1.2960953.
[42] M. Aslam, G.P. Torrence, E.G. Zey, Esterification, in: Kirk-Othmer Encyclopedia of Chemical Technology, John Wiley & Sons, Ltd, 2000. https://doi.org/10.1002/0471238961.0519200501191201.a01.
[43] M. Jagodzinski, A. Breitbart, M. Wehmeier, E. Hesse, C. Haasper, C. Krettek, J. Zeichen, S. Hankemeier, Influence of perfusion and cyclic compression on proliferation and differentiation of bone marrow stromal cells in 3-dimensional culture, Journal of Biomechanics. 41 (2008) 1885–1891. https://doi.org/10.1016/j.jbiomech.2008.04.001.
[44] J.C. Hu, K.A. Athanasiou, The effects of intermittent hydrostatic pressure on self-assembled articular cartilage constructs, Tissue Eng. 12 (2006) 1337–1344. https://doi.org/10.1089/ten.2006.12.1337.
[45] C.V. Maduka, M. Alhaj, E. Ural, M.M. Kuhnert, O.M. Habeeb, A.L. Schilmiller, K.D. Hankenson, S.B. Goodman, R. Narayan, C.H. Contag, Stereochemistry Determines Immune Cellular Responses to Polylactide Implants, ACS Biomater. Sci. Eng. (2023). https://doi.org/10.1021/acsbiomaterials.2c01279.
[46] A.A. Ignatius, L.E. Claes, In vitro biocompatibility of bioresorbable polymers: poly(L, DL-lactide) and poly(L-lactide-co-glycolide), Biomaterials. 17 (1996) 831–839. https://doi.org/10.1016/0142-9612(96)81421-9.

[47] B. Ruellan, I. Jeanneau, F. Canevet, F. Mortier, E. Robin, Fatigue of natural rubber under different temperatures, International Journal of Fatigue. (2018). https://doi.org/10.1016/j.ijfatigue.2018.10.009.
[48] C. Cruanes, G. Berton, F. Lacroix, S. Méo, M. Ranganathan, Study of the fatigue behavior of the chloroprene rubber for uniaxial tests with infrared method, Elastomery. 2 (2014) 3.
[49] C.-M. Ho, N.S. Nosseir, Dynamics of an impinging jet. Part 1. The feedback phenomenon, Journal of Fluid Mechanics. 105 (1981) 119–142. https://doi.org/10.1017/S0022112081003133.
[50] B. Hu, H. Wang, J. Liu, Y. Zhu, C. Wang, J. Ge, Y. Zhang, A Numerical Study of a Submerged Water Jet Impinging on a Stationary Wall, Journal of Marine Science and Engineering. 10 (2022) 228. https://doi.org/10.3390/jmse10020228.